

# Unsupervised Hyperspectral Segmentation on Placenta Database

Alvaro Flores-Romero  
*alvarofl@stud.ntnu.no*

Kang Yuan  
*kangyuan@student.uef.fi*

Austin Ryan English  
*aenglish@student.uef.fi*

Akash Harijan  
*akashari@student.uef.fi*

Ali Raza Syed  
*alirsyed@student.uef.fi*

**Abstract**—It is possible to obtain the spectral signature of a tissue type with a hyperspectral camera. Devices like this allow to study features in a spatial range that wouldn't be captured otherwise. Because each particular tissue behaves differently it is possible to understand and model this differences to classify and segment pixels on a hyperspectral image. In this work we explore different classical and deep learning based approaches for the problem of unsupervised hyperspectral segmentation of placenta database. Although the inspiration for techniques are mainly derived based on the placenta database, the techniques are potentially general enough to be applicable to other medical and non-medical hyperspectral images of different databases. Computational complexity was reduced with dimensionality reduction methods such as Optimal Combination Strategy (OCS) and Principal Component Analysis (PCA). After performing external validation, we observe that some classes consistently perform better than others. The downgraded performance on some classes are because of the high similarity between their reflectance features. Furthermore, an annotation application is developed which allows the annotator to get an initial estimation of the segmentation results which he can then modify with different tools and save in the database.

**Index Terms**—hyperspectral, unsupervised, classification

## I. INTRODUCTION

Biological and clinical studies can be extended with the help of spectral imaging on different types of tissues. Spectral imaging combines the use of spectroscopy and color imaging to extract new information. Spectroscopy measures a range of intensities corresponding to electromagnetic power at each wavelengths in the covered range. .

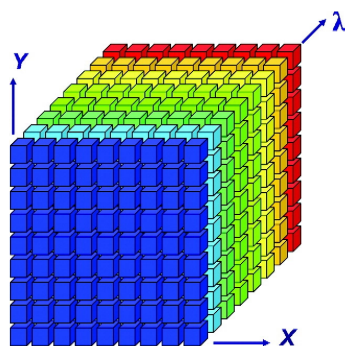


Fig. 1: Spectral cube representation [4]

Standard color imaging provides a wider spatial coverage but compromises on spectral resolution, giving normally three intensity values per pixel that ideally correspond to how the human visual system perceives colors. Spectral imaging combines imaging and spectroscopy to provide a stack of monochromatic images corresponding to a range of wavelengths as shown in Fig. 1, where  $X$  and  $Y$  correspond to the spatial domain and  $\lambda$  corresponds to the spectra captured [4].

Depending on the application, the range of wavelengths covered can be either minimalistic with very high spectral resolution or the range can be high but compromising on the spectral detail. With respect to this, although there exists no definite differentiation between ranges groups, the spectral ranges can be roughly divided into four categories as mentioned in Table I

Name	Range (nm)
Ultraviolet	200 to 400
Visible	400 to 780
Near-infrared	780 to 2,500
Mid-infrared	2,500 to 25,000

TABLE I: Spectral ranges nomenclature

Over the years, medical hyperspectral imaging has been proven to have a great value, not just for improving existing methodologies but also for devising novel methods, providing new insight into medical research fields and existing medical system features. For example, in studies on imaging systems for retinopathies, a new system was described for oximetry measurement in retinal vessels [8]. They use a modified setup of a mydriatic fundus camera with a liquid crystal tunable filter (LCTF) to capture images between 500nm and 600nm at an interval of 2nm. This is a measurement which would be extremely invasive and unlikely to be performed without medical imaging innovations such as this.

This report explores the techniques of unsupervised hyperspectral segmentation on the placenta hyperspectral image database. The total number of spectral images is 107 whereas the masks are provided for only 79 of them (a very limited ground truth). These masks are used for the external

validation of the proposed methods in an objective way. There are 11 classes in total named Artery, Artery, ICG, Blue dye, ICG, Red dye, Specular reflection, Stroma, Stroma ICG, Suture, Umbilical cord, and Vein.

Results are satisfactory allowing to initially differentiate up to 8 base classes on each hyperspectral image and use the state of the art medical graphical user interface to merge them with the help of human supervision. Intervention for this final step allows for generalization and to not underestimate the number of existing real classes.

## II. METHODS

### A. Techniques for faster and more accurate results

One of the advantages of hyperspectral images is the number of additional information obtained with the added number of bands; however, this also becomes a computational disadvantage as it makes processing extremely computationally expensive. To reduce the computational cost without greatly compromising segmentation accuracy, some of our methods use two pre-processing techniques. These techniques are described below.

*1) Optimal band selection:* Selecting particular bands of a hyperspectral method is a popular technique that allows to reduce the size of a hypercube, reducing the complexity of models and doing that in a manner which ideally enhance the good features in our application or at least minimizing the loss of information. Taking this criteria into consideration, the method developed by [7] was implemented in this project from scratch.

Band-selection is particularly different than dimensionality reduction techniques like principal component analysis (PCA) because we are still in the same feature space as our data. So in band-selection we do not lose the physical meaning of our feature space. This allows us more freedom in fine-tuning the methods according to our understanding of the physical problem [7].

The used method called Optimal Combination Strategy (OCS) relies in splitting the hyperspectral bands in M groups as shown in Figure 2). This first coarse grouping separates the bands into nearly-equal spaced segments. This ensures the global decision making while selecting particular bands which also takes into account the information shared between different bands.

After this first stage, it is required to modify the sub-groups with a fine grouping method. This is required as the coarse subsets do not group bands based on similarity. A local density band metric is implemented by [7], to determine the similarity between the bands. This was done in a sequence of steps:

- 1) The similarity matrix  $S$  is calculated between each band with its Euclidean distance where  $S \in \mathbf{R}^{L \times L}$  and  $L$  is the number of bands.

- 2) A band threshold  $\sigma \in \mathbf{R}^L$  is calculated using the similarity matrix ordered per column.
- 3) The local density  $\mu$  can then be calculated per band with the number of bands  $n$  that are below the threshold  $\sigma$ .

The limit of the coarse subset can be moved next to the band with the least density. This process can be repeated for each one of the coarse groups so they can be refined based on the density.

After this, two candidate bands from each one of the refined sub-groupings are selected. The selected bands are based on the highest entropy  $H$  of each band and the lower similarity matrix  $S$ . Finally the proposed algorithm is used to iterate through the candidate bands and select the optimal bands.

*2) Eigen images:* In some methods we also use PCA for reducing the dimensionality of the data. This not only helps in better visualization of the data but also proves better in doing classification and segmentation tasks. Although the idea of applying PCA is for individual point samples, but this can be extended to images. We can first get principal components treating each pixel spectrum as a sample. Then with those principle components we can get the dot product of principal components with the hyperspectral cube to get eigen images.

*3) Feature Agglomeration:* Feature agglomeration [3] is also a dimensional reduction algorithm that we have explored to see whether we can get better results with it. It is a hierarchical clustering based technique that starts as treating each feature as single cluster and then combines the similar features with respect to a tree based representation of features called dendrogram. Then this tree-based representation (dendrogram) is cut at certain height of tree according to the needed number of reduced features.

### B. Segmentation Methods

After testing different methods with several different parameters, we finally propose four methods for the segmentation task:

*1) Vanilla K-Means (V-KM):* K-means is a general clustering method with a good trade off between clustering accuracy and computational complexity. It seeks to minimize the Euclidean distance between points in the same cluster [2]. This is the vanilla version of K-Means. The only difference is the preprocessing of the spectral image that we do using OCS where we select 11 optimal bands to work with.

*2) K-Means with Features Agglomeration (FA-KM):* This is also another version of vanilla K-Means that was applied on feature by feature agglomeration based dimensional reduction from 37 dimensions to 3 dimensions.

*3) Spectral K-Means (S-KM):* Spectral clustering applies clustering method on the projection of a normalized Laplacian. The 'spectral' here does not mean spectral in wavelengths but spectral refer to the eigen-values of the similarity matrix created for dimensionality reduction. Spectral clustering helps where the clustering can not be performed with the measure of spread or mean of the cluster values. Taking inspiration from [2] which works on three-channel images, we implement

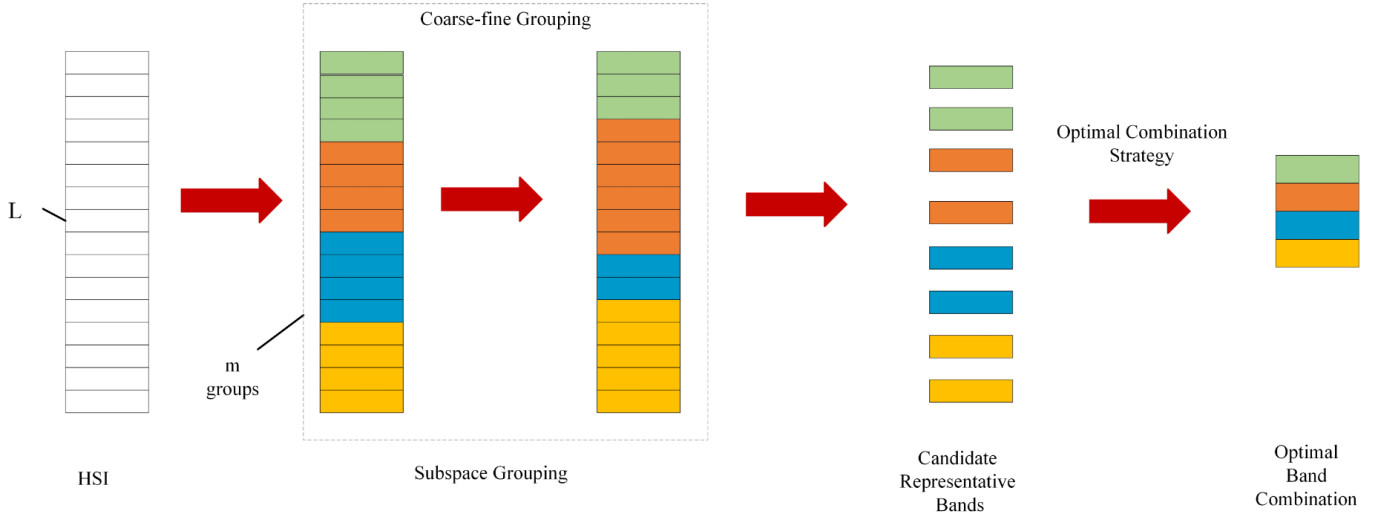


Fig. 2: Band Selection Diagram from [7]

spectral clustering with the addition that now we provide the method with optimally selected 11 bands and also add the spatial coordinates of pixels as feature. We also normalize our feature space because of the combination of the spatial coordinates with spectral values.

*4) Deep learning-based cluster segmentation (Variant 1) (DLC-V1):* We implement the approach for deep learning-based cluster segmentation for three-channel images from [6]. The parameters that we fix at the beginning is the minimum number of clusters that can exist. We fix that at the beginning of the algorithm. At the beginning the network assumes that every pixel is a separate cluster. The spectral image input is then fed into a three-layered convolutional neural network which reduces each pixel to a set of probability of belonging of each pixel to a class (30 in our case). For the loss functions, we define two of them. The first one is calculated as the difference of clusters from the single-cluster ideal image where the whole image belong to a single cluster (cluster number is randomly selected). This loss function definition allows us to optimize the network by merging pixels to match the ideal single-cluster image. This allows us to reduce the number of clusters in the image. The other loss function is defined by moving a window for each pixel in the image and comparing the window with shifted version of itself. The higher the difference of the window with its shifted version, the higher the loss. This makes the network to penalize non-convex distribution of the clusters.

*5) Deep learning-based cluster segmentation (Variant 2) (DLC-V2):* This approach is inspired from DLC-V1 which works on three-channel images. This variant is similar to II-B4 with the only difference that we provide the network with a preprocessed input from simple linear iterative clustering (SLIC) [1] for generating superpixels. Superpixels allows a headstart to the network with already formed clusters.

*6) ResUnet based deep model (DLR):* In order to solve the road extraction task, [12] proposed the deep residual U-Net

(ResUnet), an architecture that takes advantage of strengths from both deep residual learning and U-Net architecture. ResUnet not only inherits the advantages of utilizing an identity mapping to facilitate training from the residual network [5], but also inherits the advantages of combining low level detail information and high level semantic information from U-Net [11].

Based on the ResUnet architecture, we propose a total of three derivative models based on the need of exploring efficient methods with a good trade-off between accuracy and computational cost.

- *Variant 1 (DLR-V1):* This model is trained on all the 37 bands of the images.
- *Variant 2 (DLR-V2):* For this model the input is first preprocessed to provide three principal components for each hyperspectral image. For the prediction, first the three principal components are calculated for the test image and then given as an input to network. One characteristic thing to note about this method is that the principal components of each image are not associated with each other. This reduced the computational burden of the algorithm.
- *Variant 3 (DLR-V3):* For this model, the input is preprocessed to obtain three principal components for the whole dataset. This is in contrast to Variant 2 where each image had its own set of principal components. In this model, the test image is also projected to the same principal components that we got from the training phase. This allows the model to benefit on the shared hidden features in the hyperspectral images which is beneficial for improving the accuracy of the model prediction. The main disadvantage of this approach is that it requires more computing resources during the prediction phase because the training data is to be loaded again to get the principal components.

### C. Metrics for evaluation

Since visual judgments may not always be a good approach for determining whether the segmentation is working good or not. We implemented some metrics which could give us numerical results for how good the clustering performed.

We can define some parameters to be used in evaluation metrics. These parameters are True positives TP, False positives FP, False negatives FN, and True negatives TN [9].

Considering **C** is the set of predicted clusters and **GT** is the set of ground-truth classes:

**TP:** The number of data pairs found in the same cluster, in both **C** and **GT**.

**FP:** The number of data pairs found in the same cluster in **C** but in different classes in **GT**.

**FN:** The number of data pairs found in different clusters in **C** but same classes in **GT**.

**TN:** The number of data pairs found in different clusters both in **C** and **GT**.

**m1:** Total number of pairs found in the same **C**:  $TP + FP$

**m2:** Total number of pairs found in the same **GT**:  $TP + FN$

Based on the parameters defined previously we can define these metrics:

**Precision:** Counts true positives that how many examples are properly included in the same class in **GT**

$$\frac{TP}{m1}$$

**Recall:** Percentage of elements that are properly included in the same cluster in **C**

$$\frac{TP}{m2}$$

**F-measure:** combines precision and recall

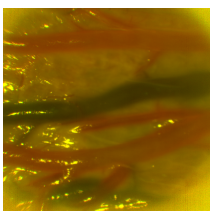
$$\frac{1 + \alpha}{\frac{1}{Precision} + \frac{\alpha}{Recall}}$$

## III. EXPERIMENTS

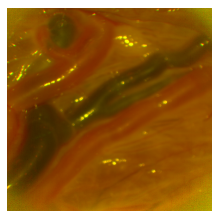
### A. Placenta Segmentation

Three images were selected randomly for the testing of the implemented models: Set 1, upper 2, icg, Set 1, lower 3, and Set 1, lower 6, icg.

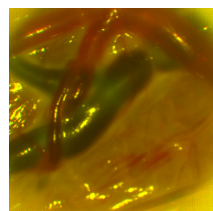
Keep in mind that in the following masks the purple and the blue masks are usually marked as a single one, but we separated them for visualization but both should be considered as a single specularity.



(a) Set 1, upper 6, icg

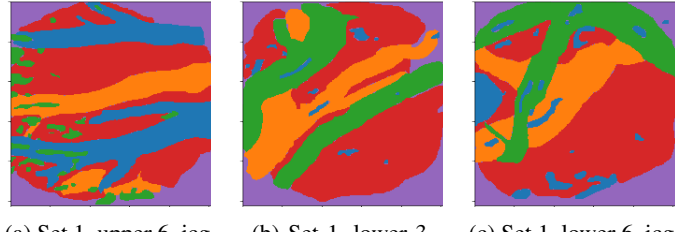


(b) Set 1, lower 3



(c) Set 1, lower 6, icg

Fig. 3: Real Images from Data



(a) Set 1, upper 6, icg      (b) Set 1, lower 3      (c) Set 1, lower 6, icg

Fig. 4: Ground Truth of selected Images

The only modification that will be done is the merging of masks. Since unsupervised segmentation is a method that can have an unknown number of labels, we decided to go for the approach of slightly over estimating the number of tissue types and then merging them on the user interface. After testing we found that it is easier to merge masks than to split them if we account for less.

### B. Manual Annotation Corrections

As part of this study, an annotation application was built for manually manipulating segmentation results with experts where needed. The functionality it provides is summarized below:

#### Annotation App Features

- Delete database images
- View mask overlays
- Create new segmentation masks
- Trigger auto-segmentation for an image
- Delete unnecessary segmentation masks
- Edit to correct existing segmentation masks
- Merge segmentation masks

As the source code involves other teams' work, contact the authors for access to the source code until it becomes available publicly. A screenshot of an example annotation browsing view can be seen in Figure 5 and an example of the editing view in Figure 6. A simple overall system diagram can be seen in Figure 7 which visualizes the connections among the various systems in the annotation application.

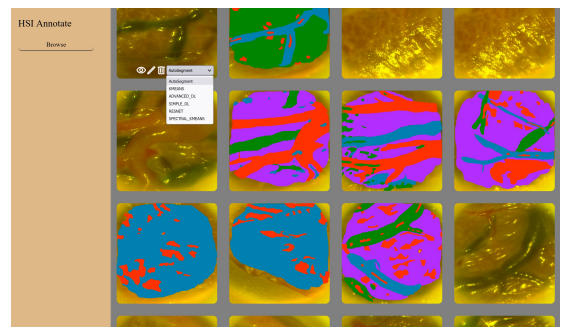


Fig. 5: Annotation application image browsing view



Fig. 6: Annotation application mask editing view

The GUI application is built in JavaScript and HTML as an easily accessible web app, using the Angular 13 framework for the user interface and Django services for managing database structures for spectral image associations. The database and services are a borrowed implementation from Team 1, based off of the hyperspectral database design specified in previous work [10]. The interface was used in conjunction with the unsupervised mask estimations. Because it is a blind problem the decision of slightly estimating more classes than the real ones was taken. This is to account for non-homogeneity and noise during the capture process (for which we have no control over). These additional classes will be merged in the tool and the results of the merging is what will be evaluated.

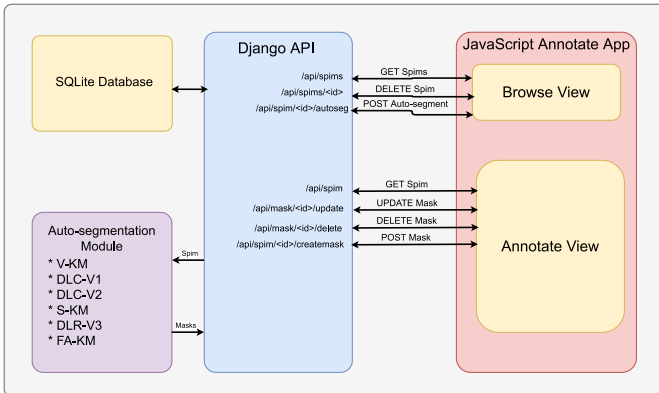


Fig. 7: Annotation application system

### C. Generalization Experiments

To evaluate the results on other datasets, hyperspectral images from other scenes were used on some of our methods. Two hyperspectral images were selected: 1) a "White Powder" HSI and 2) a "Real and Fake Leaves" HSI as it can be seen in its RGB representation in Figures 8 and 9.



Fig. 8: RGB Scene of Real and Plastic Leaves in Specim VIS Range.

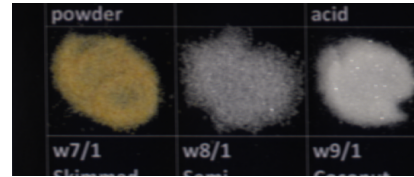


Fig. 9: RGB Scene of Powders in Specim VIS Range.

## IV. RESULTS

The results for the different segmentation methods are shown in Fig. 10-13. The used parameters used for each method can be found in the footer of each image. The abbreviations meaning is the following:

- NC = Number of Clusters
- Comb. = Combination
- PMC = Pixel mini cluster

The summary of metrics is found in Tables II-V. For these the color of the header matches the color of the original ground truth. The purple and the blue masks should be merged (covering noise and specular reflections as a single *not useful* class) and it is included in the blue column.

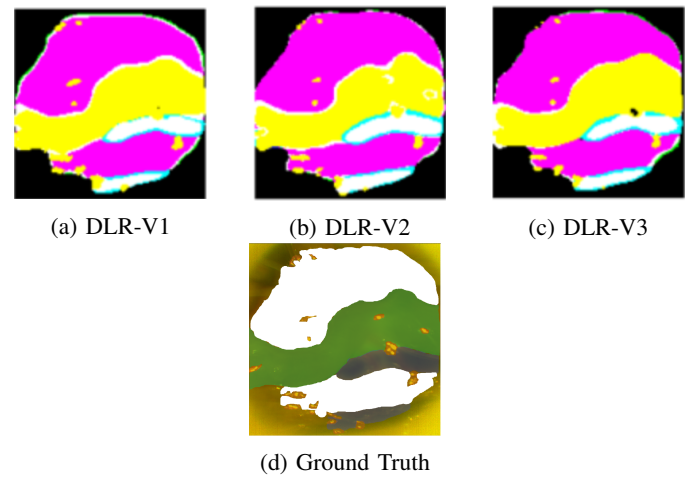


Fig. 10: DLR methods results on Set 1, upper 2, icg

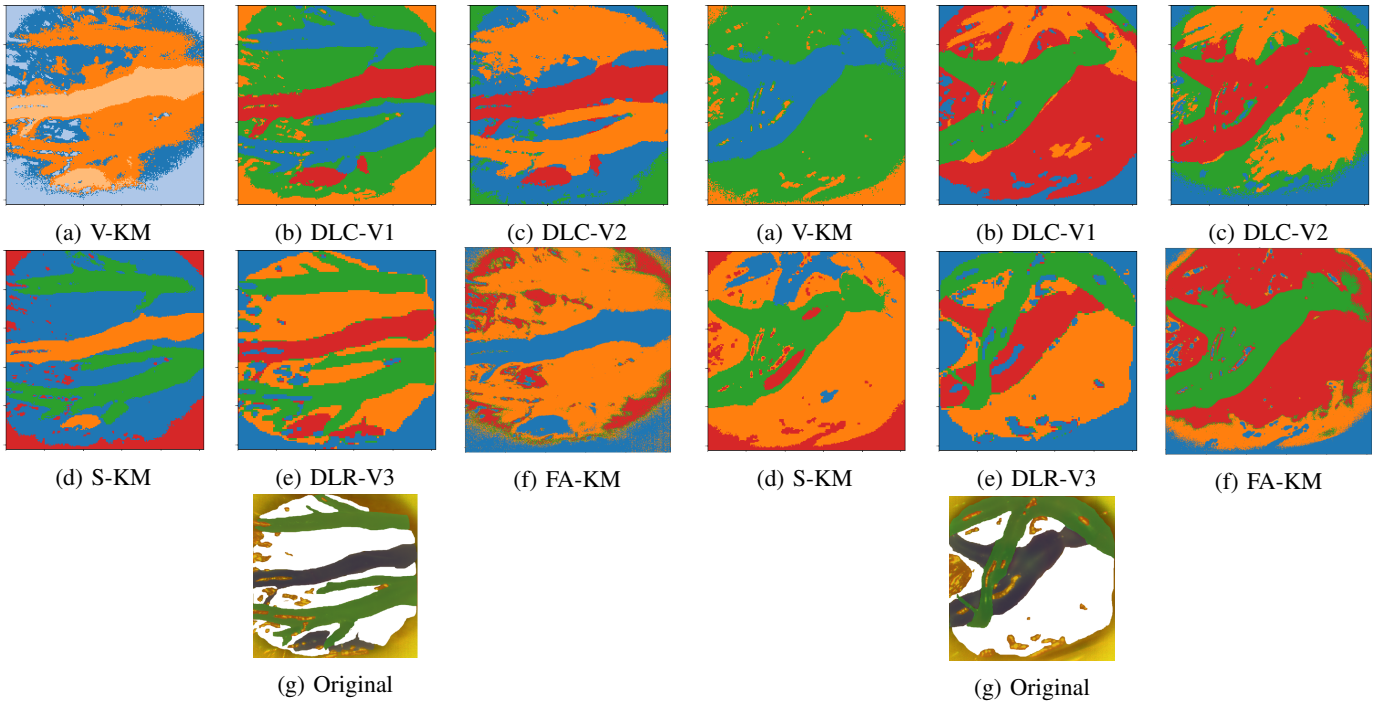


Fig. 11: Segmentation Results for "Set 1, upper 6, icg" test image. Parameters for the methods are: (11a) NC = 10 (11b) NC = 8. Comb. = 0 (11c) NC = 7, PMC = 2 (11d) NC = 10 (11f) NC=10.

Fig. 13: Segmentation Results for "Set 1, lower 6, icg" test image. Parameters for the methods are: (13a) NC = 8 (13b) NC = 8. Comb. = 1 (13c) NC = 7, PMC = 40 (13d) NC = 10 (13f) NC=10.

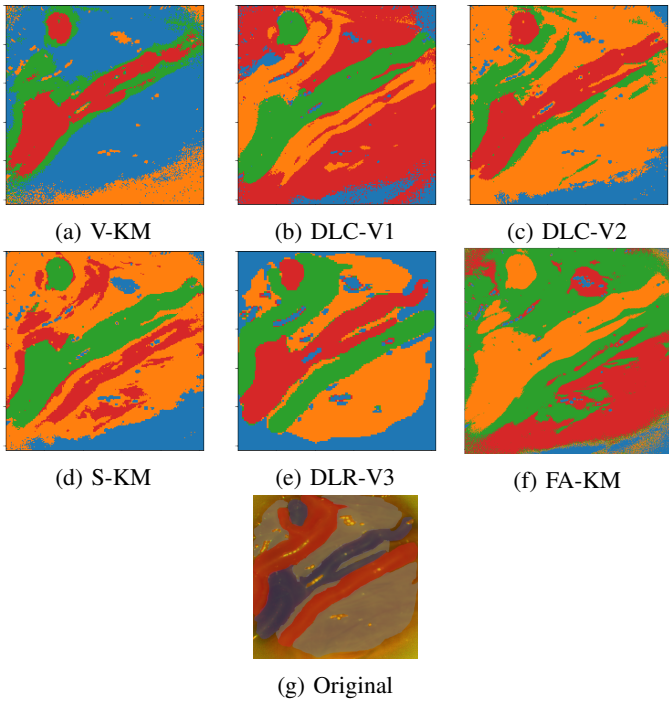


Fig. 12: Segmentation Results for "Set 1, lower 3" test image. Parameters for the methods are: (12a) NC = 8 (12b) NC = 8. Comb. = 7 (12c) NC = 7, PMC = 20 (12d) NC = 10 (12f) NC=10.

#### A. Generalization

The results of non-placenta images can be found in Figures 14 and 15.

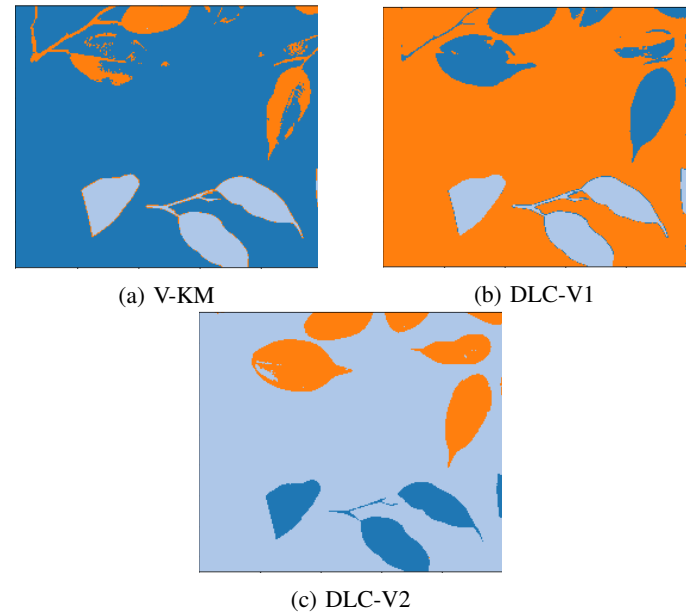


Fig. 14: Segmentation of Leaves HSI. Parameters for the methods are: (14a) NC = 8 (14b) NC = 8. Comb. = 3 (14c) NC = 8, PMC = 10

Vein			Artery, ICG			Stroma, ICG			Specular reflection			
Precision	Recall	F-Meas	Precision	Recall	F-Meas	Precision	Recall	F-Meas	Precision	Recall	F-Meas	
V-KM	0.953	0.931	0.942	0.753	0.646	0.695	0.580	0.681	0.626	0.827	0.871	0.848
DLC-V1	0.941	0.900	0.920	0.903	0.927	0.915	0.711	0.680	0.695	0.800	0.942	0.865
DLC-V2	0.937	0.877	0.906	0.831	0.712	0.767	0.604	0.631	0.617	0.739	0.956	0.834
FA-KM	0.934	0.974	0.954	0.889	0.926	0.907	0.703	0.667	0.684	0.775	0.952	0.855
DLR-V3	0.973	0.976	0.974	0.946	0.919	0.933	0.891	0.921	0.906	0.956	0.955	0.956
FA-KM	0.925	0.947	0.936	0.703	0.588	0.640	0.516	0.542	0.529	0.781	0.909	0.841

TABLE II: Segmentation results for Set 1, upper 2, icg

Vein			Artery			Stroma			Specular reflection			
Precision	Recall	F-Meas	Precision	Recall	F-Meas	Precision	Recall	F-Meas	Precision	Recall	F-Meas	
V-KM	0.921	0.967	0.943	0.654	0.746	0.697	0.587	0.567	0.577	0.811	0.891	0.850
DLC-V1	0.963	0.926	0.944	0.859	0.885	0.872	0.679	0.652	0.665	0.753	0.931	0.832
DLC-V2	0.961	0.938	0.950	0.749	0.883	0.811	0.624	0.605	0.615	0.778	0.911	0.839
S-KM	0.963	0.935	0.949	0.750	0.840	0.792	0.588	0.565	0.576	0.778	0.858	0.816
DLR-V3	0.981	0.969	0.975	0.955	0.958	0.956	0.822	0.888	0.854	0.946	0.862	0.902
FA-KM	0.852	0.950	0.899	0.575	0.717	0.639	0.701	0.597	0.645	0.903	0.971	0.936

TABLE III: Segmentation results for Set 1, lower 3

Vein			Artery, ICG			Stroma, ICG			Specular reflection			
Precision	Recall	F-Meas	Precision	Recall	F-Meas	Precision	Recall	F-Meas	Precision	Recall	F-Meas	
V-KM	0.937	0.808	0.868	0	0	0	0.607	0.637	0.622	0.750	0.958	0.842
DLC-V1	0.946	0.814	0.875	0.819	0.915	0.864	0.773	0.745	0.759	0.789	0.951	0.863
DLC-V2	0.909	0.744	0.818	0.707	0.618	0.659	0.578	0.672	0.622	0.801	0.933	0.862
S-KM	0.910	0.817	0.861	0.736	0.959	0.833	0.703	0.686	0.694	0.772	0.917	0.838
DLR-V3	0.975	0.972	0.973	0.964	0.947	0.955	0.884	0.924	0.904	0.947	0.904	0.925
FA-KM	0.763	0.926	0.837	0.702	0.634	0.666	0.549	0.569	0.559	0.966	0.857	0.908

TABLE IV: Segmentation results for Set 1, lower 6, icg

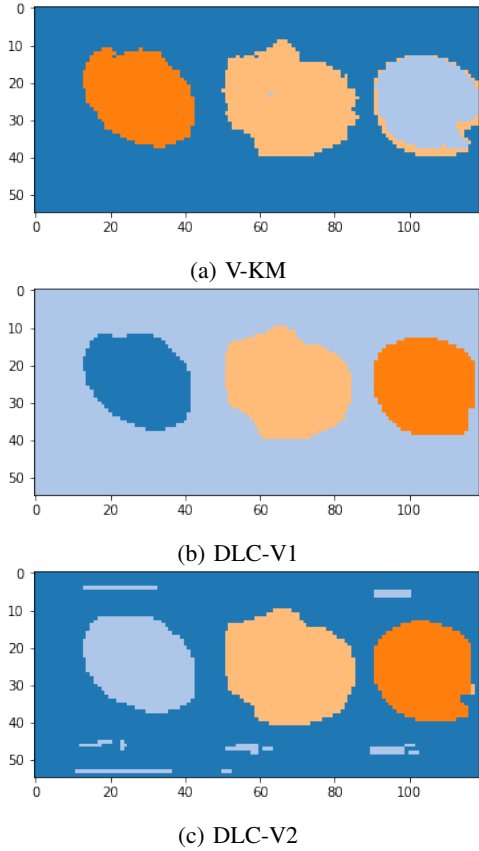


Fig. 15: Segmentation of Powders HSI. Parameters for the methods are: (15a) NC = 7 (15b) NC = 5. Comb. = 3 (15c) NC = 5, PMC = 4

	Vein	Artery, ICG	Stroma, ICG	Specular Reflection
Set 1, upper 2, icg	Avg	0.939	0.809	0.676
	Max	0.974	0.933	0.906
	Min	0.906	0.64	0.529
Set 1, lower 3	Avg	0.943	0.794	0.655
	Max	0.975	0.956	0.854
	Min	0.899	0.639	0.576
Set 1, lower 6, icg	Avg	0.872	0.662	0.69
	Max	0.973	0.955	0.904
	Min	0.818	0	0.559

TABLE V: F-Measure Summary results for tested images

## V. DISCUSSION

As shown in Tables. II-IV, we see a consistent good performance of our methods for Vein and Specular reflections. The results are summarized in Table V where the average F-Measure for these two tissues is close to 90%. In the same table it can be seen a slightly lower metric score achieved for Artery and Stroma. This can be ascribed to the very close resemblance of the reflectance spectra of both of these tissue. This can be seen in the average reflectance of tissues across all of the images in database shown in Fig.16.

It is important to mention that not only the particularities of each tissue have an impact on the accuracy of the segmentation but also does the variations across measurements (reasons unknown for the dataset used). In Figure 17 we can see that

for the entire dataset there is a big difference in measurements across images. All of the images used are flat-fielded corrected so the variation cannot be assumed to uneven light distribution.

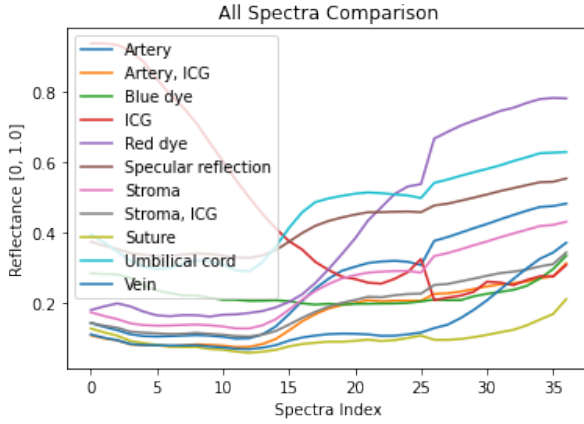


Fig. 16: Average spectra of all tissues in the database

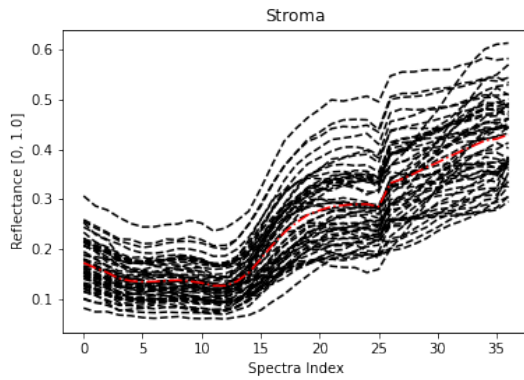
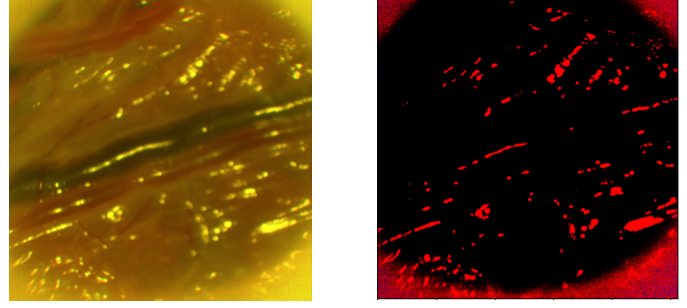


Fig. 17: Reflectance of Stroma of each image where the ground truth is known (black) with the average reflectance of the dataset (red)

For specular reflections we observe that it is being classified in the same cluster as the border noise in the images. This is consistent across all the methods. This may not be a problem because both the noise and specular reflections do not contribute in the diagnosis from the images because they contain no information. Another approach which can be taken is to remove the specular reflections and noise in the preprocessing stage. One method for detecting it is to detect outliers in the image. This can be observed in Fig.18 where the outliers are shown in a randomly selected band of the spectral image. This has shown to improve the results of some clustering methods but those methods are not discussed in this report.

Convolutional methods such as DLC-V1, DLC-V2 and DLR-V3 have more consistent results with higher accuracy than traditional machine learning methods. This can also be attributed to the feature extraction process and a better fit of



(a) Set 1, lower 10, icg

(b) Outliers

Fig. 18: "Set 1, upper 10, icg" test image

the images with such high variation (even after normalization of the images).

The annotation application used for correcting masks was built as a prototype and can be extended to interface with the hyperspectral database more closely, editing mask tissue labels and features as well as providing configurable parameters for segmentation methods triggers. Additionally, an iterating smoothing filter using morphology could be provided from the application, allowing auto-segmented results to be polished to configurable degrees and made more convex.

While working with spectral images, dimension reduction plays a huge part, currently we have explored some ways to reduce the dimensions as mentioned above but a more intelligent way of reduction will definitely make the model simpler and even increase the accuracy of models. For example in the case of OCS, it requires a manual input of the bands to be selected, but if we automate the number of segments selection and make it spectra invariant then accuracy of dependent models will improve as well. Regardless of this the reduction from 37 to 11 bands with this method has an accuracy impact of 1.2% on average for the tested images.

As it's seen, the generalization of the methods used gives (with aid of the user interface) a good segmentation results for leaves and powders which have completely different spectra than placenta tissue.

Overall the methods used build a robust tool to classify placenta images with the consideration of more classes than the available ones to enhance detail location. Manual merging of the masks by a human operator is necessary at this point of time but with further standardization of measuring techniques to reduce variation and an increasing labeled dataset, it would be able to be enhanced in the near future.

## REFERENCES

- [1] Radhakrishna Achanta et al. "SLIC Superpixels Compared to State-of-the-Art Superpixel Methods". In: *IEEE Trans. Pattern Anal. Mach. Intell.* 34.11 (May 2012), pp. 2274–2282. ISSN: 1939-3539. DOI: 10.1109/TPAMI.2012.120.

- [2] David Arthur and Sergei Vassilvitskii. “k-means++: The Advantages of Careful Seeding”. In: (), p. 11.
- [3] *FeatureAgglomeration Dimensional Reduction*. <https://scikit-learn.org/stable/modules/generated/sklearn.cluster.FeatureAgglomeration.html>. Accessed: 2022-11-30.
- [4] Yuval Garini, Ian T. Young, and George McNamara. “Spectral imaging: Principles and applications”. In: *Cytometry A* 69A.8 (Aug. 2006), pp. 735–747. ISSN: 1552-4922. DOI: 10.1002/cyto.a.20311.
- [5] Kaiming He et al. “Deep residual learning for image recognition”. In: *Proceedings of the IEEE conference on computer vision and pattern recognition*. 2016, pp. 770–778.
- [6] Wonjik Kim, Asako Kanezaki, and Masayuki Tanaka. “Unsupervised Learning of Image Segmentation Based on Differentiable Feature Clustering”. In: *IEEE Transactions on Image Processing* 29 (2020), pp. 8055–8068. ISSN: 1057-7149, 1941-0042. DOI: 10.1109/TIP.2020.3011269. arXiv: 2007.09990[cs]. URL: <http://arxiv.org/abs/2007.09990>.
- [7] Shuying Li et al. “Hyperspectral Band Selection via Optimal Combination Strategy”. In: *Remote Sensing* 14.12 (), p. 2858. ISSN: 2072-4292. DOI: 10.3390/rs14122858. URL: <https://www.mdpi.com/2072-4292/14/12/2858>.
- [8] D. J. Mordant et al. “Spectral imaging of the retina”. In: *Eye* 25.3 (Mar. 2011), pp. 309–320. ISSN: 1476-5454. DOI: 10.1038/eye.2010.222.
- [9] Julio-Omar Palacio-Niño and Fernando Berzal. “Evaluation Metrics for Unsupervised Learning Algorithms”. In: *arXiv* (May 2019). DOI: 10.48550/arXiv.1905.05667. eprint: 1905.05667.
- [10] Sami Puustinen et al. “Towards Clinical Hyperspectral Imaging (HSI) Standards: Initial Design for a Microneurosurgical HSI Database”. In: *2022 IEEE 35th International Symposium on Computer-Based Medical Systems (CBMS)*. IEEE. 2022, pp. 394–399.
- [11] Olaf Ronneberger, Philipp Fischer, and Thomas Brox. “U-net: Convolutional networks for biomedical image segmentation”. In: *International Conference on Medical image computing and computer-assisted intervention*. Springer. 2015, pp. 234–241.
- [12] Zhengxin Zhang, Qingjie Liu, and Yunhong Wang. “Road extraction by deep residual u-net”. In: *IEEE Geoscience and Remote Sensing Letters* 15.5 (2018), pp. 749–753.